PAPER

Check for updates

4D printed biocompatible magnetic nanocomposites toward deployable constructs†

Saswat Choudhury,[a] Akshat Joshi,[a] Debayan Dasgupta,[b] Ambarish Ghosh, [bc] Sonal Asthana[de] and Kaushik Chatterjee [*ad]

4D printing of shape memory polymers (SMPs) and composites has been realized for a multitude of applications spanning healthcare, soft robotics, environment, space, *etc.* However, demonstrating such materials for *in vivo* applications has not been possible to a large extent due to the unavailability of suitable materials with recovery temperatures at around physiological levels. Also, direct heating to trigger shape recovery in SMPs is not a practical and elegant approach in many cases. In this study, polylactide-*co*-trimethylene carbonate (PLMC), an SMP, has been endowed with magnetic iron oxide (Fe_3O_4) nanoparticles to realize remote heating under an alternating magnetic field and at temperatures around 40 °C. The PLMC–5% Fe_3O_4 composite was 3D printed into a variety of shapes, including scaffolds, fixed into pre-programmed temporary shapes to be deployed minimally invasively, and then recovered into original shapes under magnetic actuation. The extent of shape fixity (>95%) and recovery (>99%) was excellent, and the recovery time was short (<30 s). Additionally, these magnetic composites could potentially be guided to the site of deployment through permanent magnets. Both PLMC and its composites were printed in distinct regions of a single structure, deformed, and then recovered by selective and sequential stimulation by a magnetic field and heat, respectively. The materials (both PLMC and its nanocomposites) exhibited excellent *in vitro* biocompatibility and *in vivo* biocompatibility. The composite was as efficient as PLMC in supporting osteogenic differentiation of the pre-osteoblasts, as confirmed by mineral deposition *in vitro*. Thus, the 4D printed shape memory magnetic nanocomposite presented here could be an excellent candidate biomaterial for engineering deployable scaffolds and medical devices, among other implantable applications.

1. Introduction

The field of additive manufacturing has advanced rapidly and is increasingly being adapted to meet the challenging demands of various sectors, including the environment,[1] robotics,[2] healthcare,[3] *etc.* Four-dimensional (4D) printing is the latest addition to this fascinating field. It combines three-dimensional (3D) printing with smart materials. Smart materials used are typically shape-memory polymers (SMPs), which exhibit the unique property of stabilizing a temporarily deformed shape and subsequent recovery back to their original shape by the application of an external stimulus.[4] This property stems from the distinct molecular architectures of the polymers. The presence of such distinct phases in the polymer allows it to be fixed into a temporary shape by deformation (governed by netpoints or hard segments) below the transition temperature, followed by recovery into the original shape (influenced by molecular switches or soft segments) upon heating it above the transition temperature. Owing to this intrinsic property of temperature-assisted shape recovery, SMPs have been explored for various potential applications, such as soft robotics,[5] grippers,[6] self-deployable structures in space applications,[7] and biomedical applications.[8,9]

In the field of biomedicine, it is also essential that the SMP being used is biocompatible and preferably biodegradable, and has a triggering temperature in the physiological range. There exist only a handful of polymer candidates meeting these stringent requirements, such as polylactic acid[10] (PLA), polyurethanes[11] (PUs), their blends, epoxy-based thermosets,[12] *etc.* However, these materials are associated with serious

a Department of Bioengineering, Indian Institute of Science, C.V. Raman Avenue, Bangalore 560012, India. E-mail: kchatterje@iisc.ac.in; Tel: +91-80-22933408

b Centre for Nanoscience and Engineering, Indian Institute of Science, C.V. Raman Avenue, Bangalore 560012, India

c Department of Physics, Indian Institute of Science, C.V. Raman Avenue, Bangalore 560012, India

d Department of Materials Engineering, Indian Institute of Science, C.V. Raman Avenue, Bangalore 560012, India

e Department of Hepatobiliary and Multi-Organ Transplantation Surgery, Aster CMI Hospital, Bangalore 560024, India

† Electronic supplementary information (ESI) available. See DOI: https://doi.org/10.1039/d3ma00958k

drawbacks such as difficult processability, minimal recovery performance, high recovery temperatures, which limits their applicability *in vivo*, *etc.* SMPs could be useful for facilitating minimally invasive procedures, wherein the fixed and compressed shape can be deployed at the target site, and the SMP can then recover to its original shape upon specific stimulation. SMPs have been proposed for cardiovascular stents,[13] clot removal devices,[14] self-tightening wound closure devices,[15] *etc.* When the stimulus used is light, the shape memory function can be combined with laser treatment for photodynamic therapy for cancer.[16]

Polylactide-*co*-trimethylene carbonate (PLMC), a biodegradable polymer, has been explored as a versatile shape memory polymer in some studies for biomedical applications.[17] The distinct advantage is its glass transition temperature (T_g), which lies close to the physiological temperature, rendering it a promising candidate for *in vivo* applications. However, triggering shape recovery through direct heating is not feasible in many cases, particularly for *in vivo* applications requiring intraoperative stimulation. Owing to poor thermal conductivity of the polymers, the entire surrounding region must be heated up, which could take a long time and the shape change may not be uniform. Thus, athermal heating, which is possible by careful selection of the nanofillers incorporated in the polymer matrix, is a potentially viable means of exploiting the shape memory materials for remote actuation. The stimulus could be light,[18] ultrasound,[19] water,[20] microwaves,[21] *etc.* Magnetic stimulation is a potential means of remote actuation of these materials *via* indirect heating. The most popular nanofillers in this regard are iron oxide (Fe_3O_4) nanoparticles, which have an excellent inductive heating ability. Fe_3O_4 nanoparticles have far-reaching applications in biomedicine, including hyperthermia for cancer treatment,[22] magnetic resonance imaging contrast agents,[23] *etc.* These nanoparticles also have the ability to transfer energy from the radio-frequency field to surrounding media *via* heat dissipation.[24] However, utilizing Fe_3O_4 nanoparticles to activate the recovery of SMPs is barely explored. So far, one study has reported the incorporation of Fe_3O_4 in PLA and crosslinked PLA matrices to yield composites and demonstrated the shape recovery of the composites under an alternating magnetic field.[25] However, the drawback of this material is its high recovery temperature (70 °C), complex chemical modifications to crosslink PLA, difficult processability

involving solvents, high filler concentrations, *etc.* The other few studies based on PLA and Fe_3O_4 composites[26,27] are also not devoid of the mentioned drawbacks, which limit their applications *in vivo* as deployable scaffolds. There is a pressing need for materials that can integrate remote heating capabilities with lower triggering temperatures favorable for biomedical applications.

As bone tissues are among the most widely transplanted tissues, there is significant demand for engineering tissue scaffolds for the repair and regeneration of bony tissues. In the clinic, remotely deployable scaffolds could facilitate minimally-invasive procedures. Similarly, deployable scaffolds can self-fit into complex, irregular defects. For clinical success, the SMP and its composite should effectively promote osteogenesis. There are only a few reported examples of smart biomaterials for bone tissue regeneration, such as inductive heating responsive-PLA/Fe_3O_4 composites,[27] electroactive PLA-aniline trimer,[28] and PCL (poly ε caprolactone) diacrylate-based SMPs.[29] However, these reported SMPs either require extensive chemical synthesis to fabricate[28] or are not amenable to advanced techniques of manufacturing, such as 3D printing. Most of the SMPs also have markedly higher T_g than physiological levels, which risks inducing thermal necrosis of surrounding tissues, if deployed *in vivo*.[30] So far, there are few examples of studies that demonstrate SMP composites with remote heating capability near body temperature, while concurrently promoting osteogenesis, which can thereby enable the *in situ* triggering of a shape change for self-fitting bone scaffolds.

In this work, PLMC, as an SMP, was endowed with Fe_3O_4 nanoparticles to realize remote actuation through a magnetic field. PLMC–5% Fe_3O_4 composites were 3D printed *via* extrusion-based technology into simple two-dimensional (2D) shapes and 3D shapes (Fig. 1). Extrusion printing is advantageous over other modalities like direct ink writing, which requires tedious optimization and longer times for the complete removal of the solvent from the printed structures,[31] *etc.* The composites were athermally triggered under an alternating magnetic field, highlighting free as well as restrictive shape memory properties. Dual material printing was also performed to spatially lay down PLMC and its composite in specific parts of the same structure. The dual-printed structures were selectively and sequentially actuated through inductive and direct heating. The materials were tested for thermal properties,
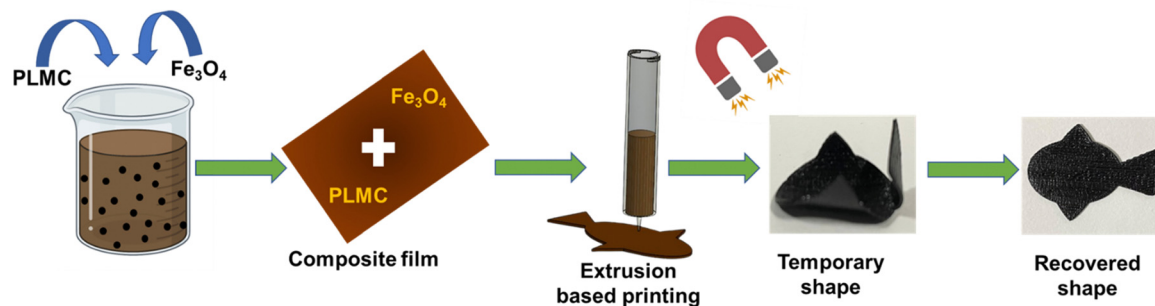

Fig. 1 Schematic of the composite preparation and 3D printing followed by magnetic actuation for shape recovery.

shape memory properties, and biological responses *in vitro* and *in vivo*. Their *in vitro* osteogenic potential was assessed toward possible applications as patient-specific, deployable biomaterials that can be remotely deployed *via* inductive heating.

2. Experimental

2.1. Materials

PLMC was purchased from Evonik Ltd, Germany. Magnetite nanoparticles (of size range of 50–100 nm) were purchased from Sigma Aldrich Pvt Ltd. Dichloromethane (DCM) of analytical grade was purchased from Sigma Aldrich.

2.2. Fabrication and 3D printing of PLMC–Fe₃O₄ nanocomposites

PLMC was dissolved in DCM (0.15 g mL^{-1}) under continuous magnetic stirring until a clear homogeneous solution was obtained. Fe$_3$O$_4$ nanoparticles were sonicated in DCM using probe sonication for about 40 min until a well-dispersed suspension was obtained. The suspension was then transferred into the polymer solution, and the resulting solution was further bath sonicated for another 40 min for the particles to homogeneously disperse in the polymer matrix. This solution was then cast over Teflon sheets and left to dry overnight. The composite film, obtained upon drying of the solvent, was then kept inside a vacuum oven for about 48 h to completely remove any traces of solvent present in the film. The obtained film was chopped into smaller uniform pieces and fed inside a metal cartridge of a 3D printer (BioX, CELLINK). The thermoplastic print head of the printer was used to facilitate melt-extrusion of the composites.

Printing parameters were optimized to get good accuracy and resolution of the composite structures. Printing temperatures were in the range from 200 °C to 210 °C. The pressure was set at 200 kPa. The printing speed ranged between 4 and 6 mm s^{-1}, depending on the complexity of the structures.

2.3. Thermal characterization

The thermal properties of the polymer and nanocomposite were characterized using differential scanning calorimetry (DSC, TA Instruments Q 2000). The samples of weight 3–5 mg were scanned between −70 °C and 200 °C at a scanning rate of 10 °C min^{-1}. The samples were subjected to a heat–cool–heat cycle to remove any processing history. Thermal degradation was performed on the samples using thermogravimetric analysis (TGA, TA Instruments Q 500). Samples of 3–5 mg were heated from 40 °C to 800 °C at a heating rate of 10 °C min^{-1} under an inert atmosphere.

2.4. Shape-memory characterization

Shape memory properties of both the 3D printed polymer and composite structures were assessed by performing a shape memory testing cycle using a TA instruments-Q800, dynamic mechanical analysis (DMA) system. The samples for this test were prepared by 3D printing the materials into rectangular strips of $25 \times 6 \times 1$ mm^3. The test was performed in a stress-controlled tension mode in the following program:

(i) Deformation: the printed sample was heated to a temperature T_d (deformation temperature slightly above T_g) and equilibrated for 5 min with a preload of 0.005 N, which gives the initial strain ($\varepsilon_{\text{initial}}$). The sample was then stretched isothermally from 0.001 to 0.025 MPa with a stress ramp rate of 0.005 MPa min^{-1}. The strain at this point was denoted as deformed strain ($\varepsilon_{\text{deformed}}$).

(ii) Cooling: the sample was then cooled to 0 °C (much below T_g) at a rate of 5 °C min^{-1}. It was equilibrated for 5 min under the application of constant stress.

(iii) Fixing: the external stress was unloaded isothermally at a rate of 0.005 MPa min^{-1}. It was again equilibrated at 0 °C for 5 min, and the strain captured at this point was fixed strain (ε_{fix}).

(iv) Recovery: the sample was reheated at a rate of 5 °C min^{-1} to T_d and equilibrated for 10 min. The recorded strain is indicated as the residual strain after recovery ($\varepsilon_{\text{recov}}$). The sample was finally cooled down to 0 °C.

$$R_f \ (\%) = \frac{\varepsilon_{\text{fix}}}{\varepsilon_{\text{deformed}}} \times 100\%$$

$$R_r \ (\%) = \frac{\varepsilon_{\text{deformed}} - \varepsilon_{\text{recov}}}{\varepsilon_{\text{deformed}} - \varepsilon_{\text{initial}}} \times 100\%$$

2.5. Morphological and chemical characterization

Fe$_3$O$_4$ nanoparticles were characterized for their morphology and chemical structure using scanning electron microscopy (Ultra 55 FESEM, Karl Zeiss Mono) and X-ray diffractometry (XRD), respectively. The particles were dispersed homogeneously in ethanol before drop casting over silicon wafers, which were mounted on an aluminum stub, sputter coated with gold, and then imaged by SEM. An accelerating voltage of 4 kV and a secondary electron detector (SE2) were used for imaging.

PLMC–Fe$_3$O$_4$ composites were 3D printed into disc-shaped structures, desiccated, and gold-sputtered before visualization by SEM. The interfilament distance was measured from the micrographs and was compared with the 3D models to estimate the printing accuracy. PLMC and PLMC–Fe$_3$O$_4$ composites were characterized for chemical structure using Fourier transform infrared spectroscopy-attenuated total reflectance (FTIR-ATR) analysis by a PerkinElmer Fourier spectrometer, USA. The spectra were recorded in the range of 650–400 cm^{-1} with a resolution of 4 cm^{-1}.

2.6. Uniaxial mechanical properties

For the evaluation of the tensile mechanical properties, both PLMC and PLMC–Fe$_3$O$_4$ composites were printed into standard sized rectangular bars ($30 \times 3 \times 0.5$ mm^3) and then were subjected to a uniaxial tensile load in a dynamic mechanical analyzer using a controlled force mode. Loading rate was fixed at 1 N min^{-1}, with a preload of 0.01 N and the tests were performed at 37 °C. The obtained stress–strain plots were curve-fitted to calculate the slope of the linear region, which indicated the tensile modulus of the sample. At least three samples were tested for each set.

2.7. Magnetic field heating of the PLMC–Fe₃O₄ nanocomposites

Magnetic hyperthermic heating was achieved by using an Ambrell Easyheat Induction system (10 kW). The magnetic field generated inside the coil was kept at ≈ 40 kA m^{-1} (≈ 500 Gauss). The magnetic field oscillated at a frequency of 215 kHz. The power delivered at the center of the hyperthermia coil was kept in the range from 3.7 kW to 4.1 kW.

2.8. *In vitro* cytocompatibility

NIH-3T3 cells were cultured in DMEM high glucose cell culture media (supplemented with 10% FBS). Sterilized samples were then seeded with fibroblast cells (NIH-3T3) at 8–10 passages at a density of 10 000 cells per cm^2. Cell growth was monitored using an Alamar blue assay following the manufacturer's protocol (Thermo Fisher Scientific, USA). Cells on day 3 post seeding were also stained with Calcein-AM/Ethidium homodimer (EtDi, EthD-1; Thermo-fisher Scientific, USA) to visually analyze the toxicity of the prepared samples. The morphology of the seeded cells was also analyzed on days 3 and 5 using phalloidin (Alexa fluor 488, Thermo Fisher Scientific, USA)/DAPI (4′,6-diamidino-2-phenylindole, Thermo Fisher Scientific, USA) double staining.

2.9. Osteogenic potential assessment

MC3T3-E1 mouse calvarial pre-osteoblasts were cultured in an α-minimum essential medium (α-MEM) containing 10 vol% fetal bovine serum. The 3D printed scaffolds were UV-sterilized before seeding cells on them at a density of 7000 cells per cm^2. Cells on the scaffold surface were evaluated by live/dead assay 24 h post-seeding to qualitatively assess the viability of the seeded cells. The F-actin arrangement in the cells was evaluated by using actin and nuclear staining after 24 h. The seeded cells were first fixed with 3.7% formaldehyde. 0.1% Triton X-100 was used to permeabilize the cells. The samples were incubated with phalloidin/DAPI (6.6 μM phalloidin and 1 μg mL^{-1} DAPI) for 15 min before imaging using an epi-fluorescence microscope.

For assessing osteogenesis *in vitro*, 24 h post-seeding of the cells in the growth medium (complete culture medium as described above), the medium was replaced by an osteogenic medium (growth medium containing 10 nM dexamethasone, 50 μm ascorbic acid, and 10 mM β glycerophosphate, all Sigma Aldrich). The mineral deposition was assessed on days 7 and 14 using Alizarin red S (ARS, Sigma) dye, which binds to the calcium salts. Cells were fixed in formaldehyde, and the samples were incubated in 2% ARS solution for 40 min. The scaffolds were washed with ultrapure water and incubated in 5% sodium dodecyl sulfate (SDS) solution in 0.5 N HCL solution for 45 min. The absorbance of the dissolved stain was quantified at 405 nm using a microplate reader.

2.10. *In vivo* biocompatibility assessment

The *in vivo* toxicity of the scaffolds was assessed using Wistar rats. All the animal work was performed in accordance with the 86/609/EEC act and approved by the Institute Animal Ethics Committee of the Indian Institute of Science, Bangalore (protocol number CAF/Ethics/878/2022). Adult male Wistar rats aged 8–10 months, weighing 190–230 g, were housed in well-ventilated cages supplied with autoclaved sawdust beddings. Food and sterile water were given *ad libitum*. A 12 h light and dark cycle was maintained in the animal house at 25 ± 1 °C with $55 \pm 5\%$ humidity. The surgeries and experiments were performed in the light cycle. The animals were divided into three groups, *i.e.*, sham, PLMC, and composite scaffolds, with each group containing three animals. All the animals were anesthetized on day 15 by injecting a cocktail of 80 mg kg^{-1} ketamine and 15 mg kg^{-1} xylazine intraperitoneally. The coat around the mid-dorsal area of the anesthetized animals was shaven and sterilized with betadine, and a horizontal incision of approximately 1.5 cm was made in the skin using a sterile surgical blade to create a subcutaneous pocket. UV-sterilized scaffolds were implanted inside the subcutaneous pocket, and the incision was closed using 4.0 sutures. No implantation was done in the sham control rats. At the end of 15 days, the animals were sacrificed, and the skin tissue around the implant site was excised and preserved in formalin solution (10% in PBS). Vital organs, such as the kidneys and liver, were also taken out for evaluation and preserved in the formalin solution. The fixed tissue was then embedded in paraffin, and tissue sections of 5 μm were prepared by using a microtome. The obtained sections were stained with hematoxylin and eosin (H&E) and imaged under a light microscope (IX-53, Olympus).

To assess any inflammatory response, hematological parameters were also checked. On day 7 and day 15, 1 ml of blood was collected from each animal. The blood was collected in heparin-coated tubes for the estimation of Total Leukocyte Count (TLC), Erythrocyte Sedimentation Rate (ESR), Serum glutamic pyruvic transaminase (SGPT) and Serum Glutamic-Oxaloacetic Transaminase (SGOT).

2.11. Statistical analysis

The results are presented as mean ± standard error for each group. GraphPad Prism 5.04 was used for statistical analysis (GraphPad Software, San Diego, CA, USA). One-way ANOVA was used for the statistical analysis, which was then followed by Dunnett and Tukey tests for significance. All analyses were carried out at a 95% confidence level and were significant at statistical probability (p-value) < 0.05. Statistical significances were denoted as (*), (**), and (***) for $p < 0.05$, $p < 0.01$, and $p < 0.001$, respectively.

3. Results and discussion

PLMC typically exhibits glass transition in a broad range from 20 °C to 45 °C, depending on its molecular weight, monomer (lactide (L) : trimethylene carbonate (TMC)) ratio,[32] *etc.* The ratio of L : TMC was 70 : 30 in the copolymer used in this study. PLMC–Fe₃O₄ composites containing 2.5%, 5%, and 10% (by weight) Fe₃O₄ nanoparticles (diameter in the range of 50–100 nm) were prepared by solvent casting. 10% composites
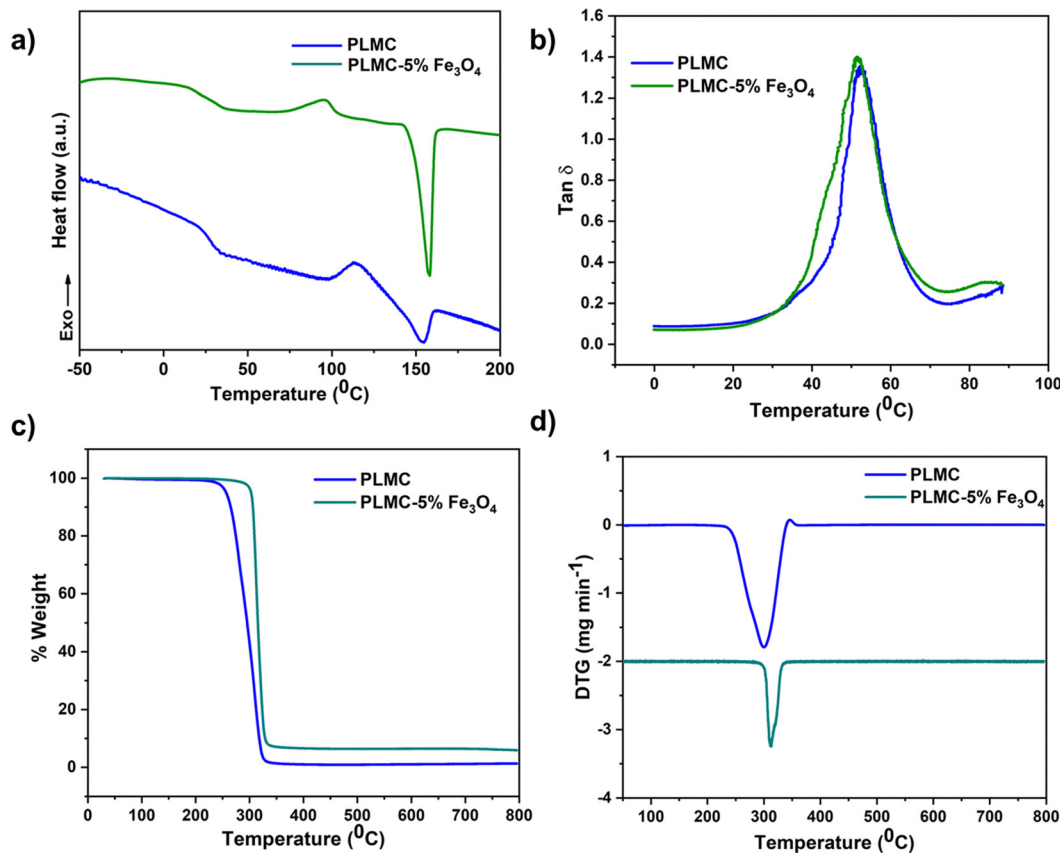
Fig. 2 Thermal and dynamic thermo-mechanical characterizations of PLMC and its composite. (a) DSC thermograms, (b) $\tan \delta$ (damping factor) as a function of temperature, (c) TGA curves, and (d) DTG curves *versus* temperature.

were difficult to print because of frequent clogging of the nozzles during printing owing to high melt viscosity. 2.5% composite structures exhibited minimal shape recoveries under a magnetic field, as the particle content was low. Hence, 5% content was determined to be optimal as it was easily processable by printing and exhibited good shape recoveries. The printing accuracy, as estimated from the SEM micrographs of the printed PLMC–5% Fe_3O_4 composites (Fig. S2(b), ESI†) was found to be $\approx 95\%$. Therefore, only the 5% composite was used for further studies.

As seen from Fig. 2(a), DSC thermograms reveal the T_g of PLMC to be ≈ 33 °C, whereas that of the PLMC–Fe_3O_4(5%) composite is marginally lower (by 3°) at ≈ 30 °C. This change is attributed to the plasticizing effect of the nanoparticles, which reduces the thermal energy required for the segmental motions of the polymer chains.[33] Both the PLMC and nanocomposites also exhibit cold crystallization (T_{cc}) at ≈ 112 °C and ≈ 95 °C, respectively, due to the formation of crystals from the quenched-in amorphous structure above T_g.[34] The lower T_{cc} in the composite suggests faster crystallization induced by the iron oxide nanofillers that act as potential nucleation sites.[35] While some studies report PLMC to be amorphous,[32] other studies indicate its semi-crystalline nature.[36] Hence, the crystallinity depends on the molecular weight, polymerization kinetics, *etc.* The PLMC used in this study did exhibit sharp

melting peaks in the DSC analysis. Melting of PLMC and the composite occurs at ≈ 158 °C, as seen from the sharp endothermic peak. The increased sharpness of the melting peak in the case of the composite can be attributed to its enhanced crystallinity due to iron oxide nanoparticles acting as nucleation sites. Neat PLMC has a relatively broader melting endotherm suggesting multiple crystallites and/or melt-recrystallization, which is common in neat polymers and has been observed earlier.[37] Fig. 2(b) reveals the $\tan \delta$ values of PLMC and its composite, as recorded from temperature sweeps performed by DMA (dynamic mechanical analysis). T_g calculated from the peak of $\tan \delta$ of PLMC is 53 °C, whereas it is 51 °C for the composite. It is to be noted that DSC captures the thermal transitions in a polymer alone, without accounting for mechanical forces, which might influence the T_g values. In contrast, DMA is a more sensitive technique that captures the mechanical vibrations inside the polymer chains along with the thermal transitions, thereby resulting in different and higher T_g values than from DSC.[38] Also, the polymer specimen remains stretched in DMA (in tension mode), whereas DSC measures the T_g of unstretched samples.[39]

The TGA (thermogravimetric analysis) results indicate that thermal degradation of PLMC starts at ≈ 240 °C, while the composite starts to degrade at ≈ 285 °C, as observed in Fig. 2(c). These data aid in determining the optimal printing temperatures and times to minimize thermal degradation of the

materials during melt extrusion-based 3D printing. TGA also confirmed the nanofiller content in the polymer matrix to be $\approx 5\%$. As observed in Fig. 2(d), the DTG (derivative thermogravimetric analysis) curves show the temperature of maximum decomposition rate for PLMC to be 300 °C and the composite to be 310 °C.

Fig. S1 (ESI†) confirms the structure of iron oxide nanoparticles from XRD and morphology from SEM. FTIR results in Fig. S2 (ESI†) show the absence of any new chemical bond formation following the incorporation of nanoparticles in the PLMC matrix. This lack of interaction is due to the absence of functionalization in the particles, which only allows physical interaction with the polymer matrix. The peaks at 1085, 1187, and 1746 cm^{-1} correspond to C–O stretching, C–C stretching, and –C=O vibration, respectively, in both neat PLMC and the composite samples corroborating the data from other studies on PLMC reported in the literature.[17] SEM images of the 3D printed composite structures confirm the excellent printability by the extrusion printing technique.

Fig. 3 compiles the shape memory characteristics of neat PLMC and its magnetic nanocomposite. As calculated from the shape memory testing routines, PLMC exhibited excellent shape fixing of $\approx 95\%$ and shape recovery of $\approx 99\%$. Similarly, the PLMC–Fe$_3$O$_4$ composite exhibited $\approx 97\%$ shape fixing and $\approx 99\%$ shape recovery. The slightly enhanced shape fixing in

the composite could be due to increased resistance in the polymer chain motions offered by the stiff nanofillers below T_g. It is to be noted that shape recovery of PLMC starts at 44 °C and the composite at 41 °C, as indicated by the shape recovery onset temperature (T_s) in Fig. 3(b) and (d). T_s can differ from T_g and indicates the temperature at which macroscopic shape recovery occurs. It can also be observed from Fig. S3 (ESI†) that the storage modulus exhibits a sharp drop with an increase in temperature. For the entire temperature range, the storage moduli (which correspond to the energy absorbed by the material) are much higher (log order) than the loss moduli (representative of the energy dissipated) for both PLMC and the PLMC–Fe$_3$O$_4$ composite, which is indicative of their dimensional stability. Also, both the storage and loss moduli of the PLMC–Fe$_3$O$_4$ composite were less compared to those of neat PLMC, which could be due to the addition of a small amount of nanofiller, which does not form a three-dimensional network, and consequently its interaction with the polymer matrix is weak. Additionally, the static mechanical properties of the neat polymer and composites were assessed by uniaxial stretching, which reveals the tensile modulus of PLMC to be higher (≈ 144 MPa) than that of the PLMC–Fe$_3$O$_4$ composite (100 MPa). This can be explained by the reduction of molecular chain entanglements caused by the addition of nanofiller, which offsets any strengthening effect.[40] Cyclic thermomechanical testing was
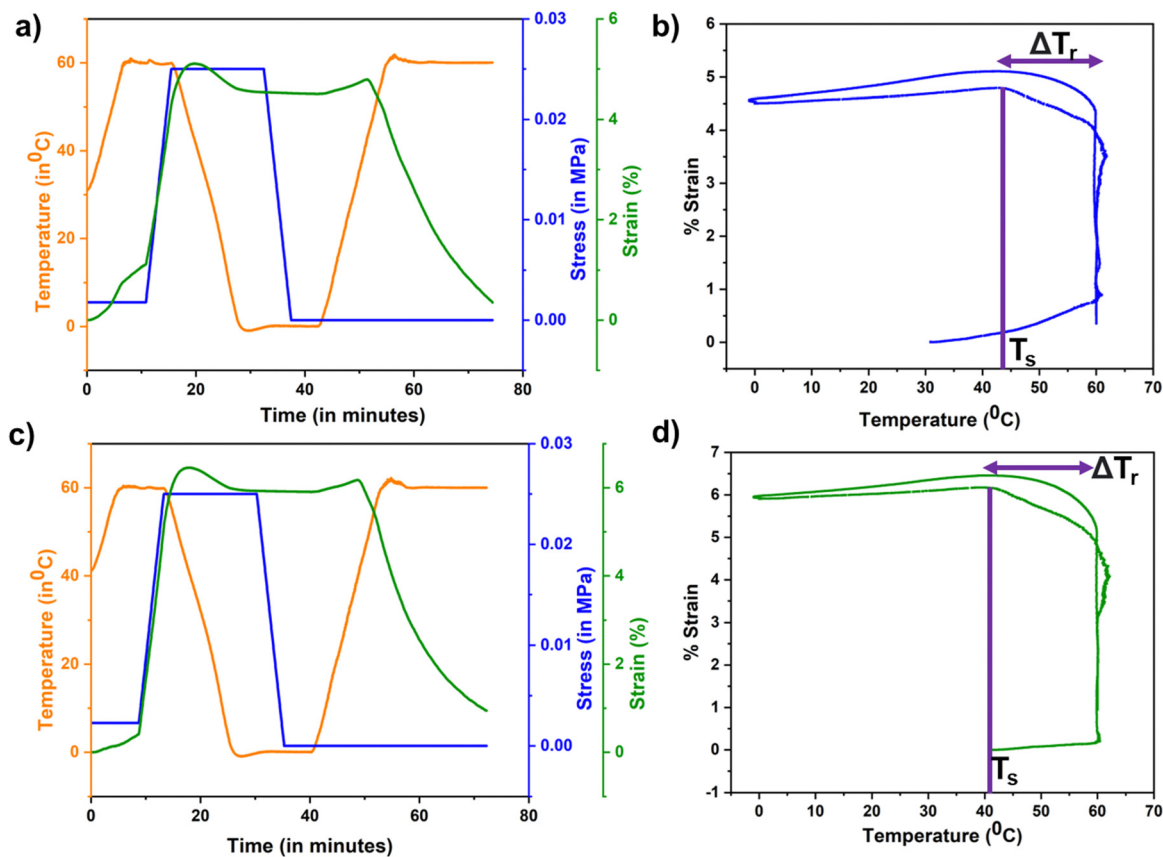

Fig. 3 Shape memory characterization of PLMC and its composite. (a) Thermomechanical shape memory testing of PLMC, (b) strain profile of PLMC with temperature, (c) thermomechanical shape memory testing of the PLMC composite, and (d) strain profile of the PLMC composite with temperature.

also performed for both materials for up to three cycles, as shown in Fig. S3 (ESI†). It is observed that PLMC sustained good fixing and recovery ratios, except for the first cycle.[41] The composite displayed excellent shape fixing and recovery ratios for the first cycle, with a reduction in the properties in the subsequent cycles. It is known that the cyclic shape memory performance is highly dependent on testing parameters such as deformation rate, fixing temperature, recovery time, *etc.*[42] Hence, these results may vary with different testing conditions.

Next, PLMC–5% Fe_3O_4 composites were 3D printed into planar (2D) shapes and fixed into temporary shapes below T_g. Upon placing them in an alternating magnetic field, they recovered back to their original shapes by inductive heating, as shown in Fig. S4 (ESI†). This is due to the fact that Fe_3O_4 nanoparticles act as localized heating sources inside the composite, and once the temperature reaches sufficiently above T_g, the composite macroscopically changes its shape to recover to its initial confirmation. The extent of recovery was around 95% for all the shapes, and the recovery time was 45 to 60 s.

3D constructs of these composites were also printed wherein specific infill patterns (rectilinear) and densities (30%) were used to lay down materials, as these infill parameters provide the highest mechanical stability and are the most common in the literature.[43] The printed 3D constructs were then subjected to thermomechanical programming; they were first deformed into a temporary shape at 40 °C ($T > T_g$), fixed at 0 °C ($T < T_g$) and then demonstrated to recover to their original shapes on

magnetic actuation ($T > T_g$). In contrast to 2D shapes, 3D constructs were able to recover much faster (under 15 s) and better (>99%), as shown in Fig. 4 and Videos V4–V6 (ESI†). This is because of a higher amount of material, which corresponds to a higher number of heating elements and a higher specific absorption rate (SAR).[44] SAR is defined as the rate of thermal energy dissipated by a material under an alternating magnetic field.[45]

The particle size, concentration, and distribution of nano-fillers in SMP directly impact the recovery performance and time.[46] Different studies report a minimum of 10 to 15 wt% of Fe_3O_4 nanoparticles in the SMP matrix to trigger sufficient inductive heating and shape recovery.[47] However, in this study, only 5 wt% concentration of nanoparticles was sufficient to realize the shape recovery in the SMP by the magnetic field. This is highly advantageous because of better dispersions, reduced agglomeration, and ease of processability. Moreover, a higher loading of nanoparticles may adversely affect cell viability and lead to additional complications *in vivo*.[48]

For *in vivo* applications, direct heating is not feasible owing to the poor thermal conductivity of polymers, which then warrants the surrounding regions to be heated high enough to trigger shape recovery. Moreover, the tissues deep inside are not accessible to trigger shape recovery through contact heating. Magnetic composites offer a potential benefit allowing for a contactless recovery through inductive heating, which is very localized in nature and does not affect the temperature of the
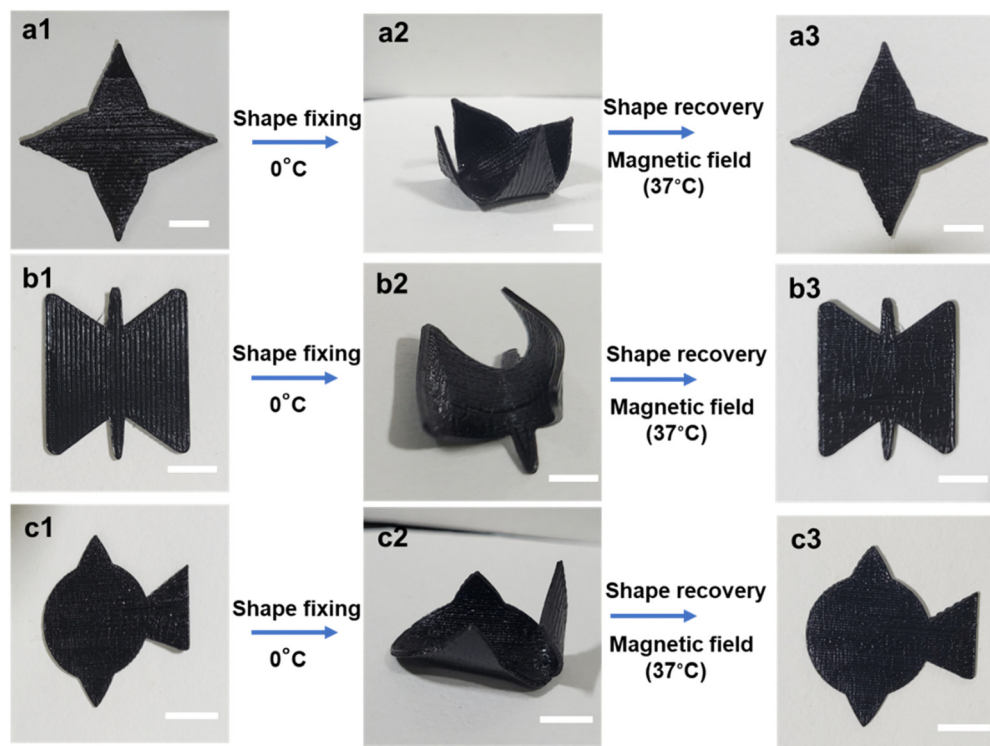

Fig. 4 Shape recovery of 3D printed PLMC–5% Fe_3O_4 (3D structures) under an alternating magnetic field; (a1) as printed petal shape, (a2) a deformed and fixed ($<T_g$) petal, and (a3) a recovered ($>T_g$) petal; (b1) as printed butterfly shape, (b2) a deformed and fixed ($<T_g$) butterfly, and (b3) a recovered ($>T_g$) butterfly; and (c1) as-printed fish shape, (c2) a deformed and fixed ($<T_g$) fish, and (c3) a recovered ($<T_g$) fish (scale: 10 mm).

neighbouring milieu and does not require heating of the neighboring tissues. Fig. 6(a) shows a 3D printed composite construct (printed using a 30% rectilinear infill pattern like a tissue scaffold), which in its original disc confirmation is not deployable. It could be easily deformed and fixed into flattened discs, which could then be delivered inside a tube. The scaffolds showed excellent shape recovery (>99%) under 15 s inside a magnetic field, as shown in Video V7 (ESI†). The corresponding thermal images in Fig. S6 (ESI†) show that the maximum temperature at the core of the scaffold is ≈40 °C after complete recovery. It is to be noted that the temperatures attained (≈40 °C) are much lower than the maximum tolerable levels reported.[49] In another case, the composites printed and fixed into tubular shapes could recover when constricted inside a glass tube within 10 s, as shown in Fig. 6(b) and Video V8 (ESI†). This proof-of-concept demonstrates the possibility of exploiting such materials as self-fitting structures for various tissues, requiring constricted deployment. Apart from offering a benign actuation strategy, magnetic composites can also be remotely guided by permanent magnets to the site of deployment, as shown in Video V8 (ESI†). However, detailed studies are warranted to further assess the *in vivo* deployability of these materials and the tissue response to inductive heating to establish them as scaffolds for tissue regeneration.

Next, neat PLMC and PLMC magnetic composites were used to print specific parts inside a single structure, as shown in Fig. 5. The inner core of the petal was printed using PLMC, while the bigger petal encasing was of the composite. The structures were deformed and fixed into pre-programmed shapes below the T_g. The outer petal printed with the composite only recovered inside an alternating magnetic field, as the neat PLMC was not an inductive-heating responsive. The partially recovered petal was stable unless a direct heating stimulus was provided when the inner petal of PLMC also began to recover, yielding completely recovered structures. This offers sequential and selective stimulation of parts in a structure. Additionally, a variety of dual component structures was evaluated for two-step shape recovery (as shown in Fig. S5 and Videos V9–V12 (ESI†) for a variety of structures). Such concepts could find use in soft robotics,[50,51] grippers,[52,53] *etc.*, wherein distinct regions of a macro-structure need to be actuated at one time.

Next, the *in vitro* biocompatibility of the materials was assessed using NIH-3T3 cells. The results of the cytocompatibility analysis are compiled in Fig. S7 (ESI†). Live/dead staining

(Fig. S7(a), ESI†) demonstrated that both PLMC and the composite did not show any toxicity to the cultured cells. Most of the cells were viable with very minimal cell death. Also, the cells adhered and proliferated in number over time on both materials, as seen from the Alamar blue assay (Fig. S7(c), ESI†), indicating excellent biocompatibility. Further, cytoskeletal staining on different days (Fig. S7(b), ESI†) demonstrates that cells could adhere and spread on the surface of the materials.

Toward their possible use as deployable bone tissue scaffolds, we studied the ability of the composite to support osteogenic differentiation. As observed from Fig. 6(d), fluorescence images of the cells stained with the live/dead stains show that the pre-osteoblasts are viable on both PLMC and its composite with minimal cell death after 24 h. Actin and nuclear staining of the cells reveals that they are well spread and exhibit their characteristic morphology (Fig. 6(e)). Mineral deposition is a late-stage marker of osteogenesis and can be visualized by staining with the ARS dye, which binds to calcium ions. ARS staining of the minerals deposited by the cells on 7 and 14 days demonstrates a steady increase in osteogenesis of the seeded pre-osteoblasts with time (Fig. 6(f)). The mineral deposition was similar on both PLMC and the composite scaffolds. These results demonstrate the favorable osteogenic potential of these composites, which could be partly attributed to their suitable mechanical properties.[54] Combined with the osteogenic potential of the PLMC–iron oxide composites, their excellent shape recovery performance through remote inductive heating near physiological temperatures makes them a promising deployable biomaterial candidate for implantable applications.

Since this nanocomposite has great potential to be extended for biomedical applications, *in vivo* biocompatibility was also assessed in Wistar rats. The results of *in vivo* biocompatibility are compiled in Fig. 7. Histological observations on different days post-implantation (days 7 and 14) demonstrated that both PLMC and the nanocomposite did not elicit any major inflammatory tissue response at the site of implantation. The surrounding skin displayed healthy physiology with a loosely packed extracellular matrix (ECM), skin appendages, and the absence of infiltrating inflammatory cells. Furthermore, to confirm the inflammatory response from scaffold remnants and/or degraded products, histological observations of two vital organs, the liver and kidneys, were also observed. As seen in Fig. 7, healthy physiology of both organs was observed with no signs of inflammation. Normal lobular morphology of the liver
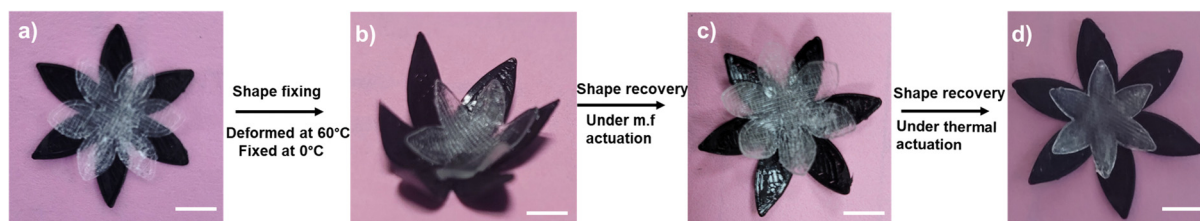

Fig. 5 Sequential and selective shape recovery of 3D printed PLMC and PLMC−5% Fe₃O₄ composite dual petal structures actuated under an alternating magnetic field and then by heat. (a) As-printed dual-printed petal with the inner petal made of PLMC and outer one of PLMC−5% Fe₃O₄ composite, (b) the deformed petal, (c) partially recovered petal by indirect inductive heating, and (d) fully recovered petal by direct heating (scale: 10 mm).
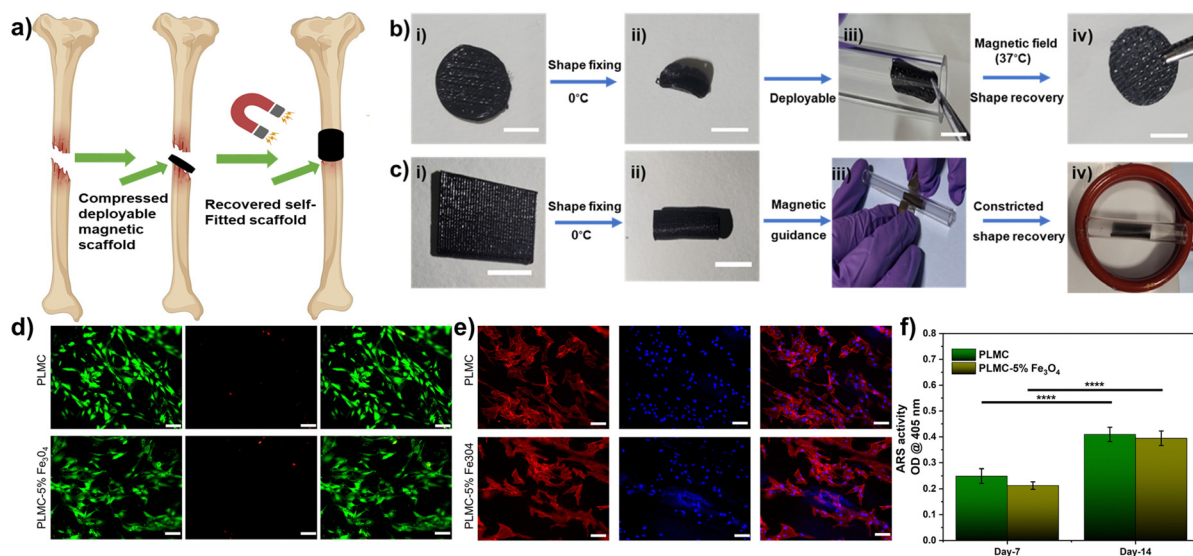
Fig. 6 Shape memory magnetic composites for use as deployable bone scaffolds. (a) Schematic highlighting the use of magnetic composites as deployable bone tissue scaffolds. (i) Tissue defect inside the human body, (ii) 3D printed composite scaffold compressed and deployed in a minimally-invasive manner, and (iii) inductive heating to trigger shape recovery of the magnetic scaffold and confirm to defect shape; (b) shape recovery of 3D printed PLMC−5% Fe_3O_4 composites as deployable tissue scaffolds under an alternating magnetic field. (i) An as-printed disc-shaped scaffold, (ii) a deformed and fixed scaffold ($<T_g$), (iii) a deformed scaffold able to be deployed through a tube, and (iv) a recovered scaffold after inductive heating (scale: 5 mm); (c) restrictive shape recovery of a pre-programmed shape to the original shape. (i) As-printed PLMC−5% Fe_3O_4 composite, (ii) a deformed and fixed shape, (iii) a magnetically guided composite, and (iv) shape recovery of the pre-programmed structure into the original shape under an alternating magnetic field (scale: 10 mm). (d) Fluorescence images of stained live (in green) and dead (in red) MC3T3 cells on 3D printed PLMC and composite scaffolds after 24 h post-seeding; (e) fluorescence images of F-actin (red) and nuclei (blue) of MC3T3 cells on 3D printed PLMC and composite scaffolds 24 h post-seeding revealing the well-spread morphology (scale: 100 μm); and (f) ARS content indicating the minerals deposited by differentiating MC3T3 cells on PLMC and the PLMC−5% Fe_3O_4 composites on days 7 and 14 (**** indicates $p < 0.0001$, one-way ANOVA).

and the characteristic kidney morphology with intact glomerulus and glomerular–capsular space in the sham, PLMC, and composite groups were observed. Furthermore, normal blood parameters in all groups confirmed the absence of any cytotoxicity induced by the implanted polymer composite over the entire period of implantation (Fig. S8, ESI†). There are several reports on the *in vivo* biodegradation of iron oxide nanoparticles and the biodistribution of degradation products.[55] It is reported that these nanoparticles tend to either accumulate in the lungs or get eliminated from circulation through liver macrophages, without any associated toxicity.[56] On the other hand, the SMP used in this study, PLMC, has been previously evaluated for *in vivo* degradation[57] and contact osteogenesis.[58] PLMC was found to slowly degrade *via* bulk hydrolysis, followed by a sterile inflammatory response and encapsulation. Since this study utilizes medical grade PLMC and a lower concentration of nanoparticles, it is envisaged that the adverse effects, if any, will be minimal and rapidly subside along with eventual safe elimination of the degraded products from the body.

There are only a few inductive heating-responsive composite systems reported earlier (as compiled in Table S1, ESI†), such as the PLMC/PTMC blend with Fe_3O_4 composites[31] and PLA–Fe_3O_4 composites.[25,27] However, the major limiting factor of all previous SMP systems is the higher T_g associated with the SMPs and the additional step of either blending[31] or crosslinking[25] to increase the shape memory efficiency. The distinct advantages

of the material system presented here include: no need for additional blending or chemical modifications, considerably less nanofiller loading (5 wt%), excellent shape recoveries of the single SMP ($>99\%$), and extremely fast (under 15 s for 3D structures) at physiological temperatures (≈ 37–$40\ ^\circ$C), which are ideal for *in vivo* deployment in biomedical applications. Extrusion-based printing was used for our work, which is advantageous as a green solvent-free fabrication technique over other strategies like direct ink writing, which involve toxic solvents and several post-processing steps. Lower filler loadings (as low as 5 wt%) were used in this study are always advantageous because of easy processability and lower risks of associated nanotoxicities.[59] The magnetic composites were printed into 3D porous scaffolds that could be potentially deployed to the site of tissue defects and triggered through inductive heating to conform to the defect size. The recovery times were short, and can be tunable by altering the nanofiller loading and/or the magnetic field strengths to suit any specific applications. Such a composite system can readily be used to securely fit relatively irregular defect sites by inductive heating-triggered remote shape change, thereby reducing the surgical challenges. *In vitro* and *in vivo* biocompatibility of PLMC and its composites was assessed to highlight the importance of the material systems as deployable tissue scaffolds. The composite was also demonstrated to display favorable osteogenic potential through increased mineral deposition over time. Additionally, PLMC
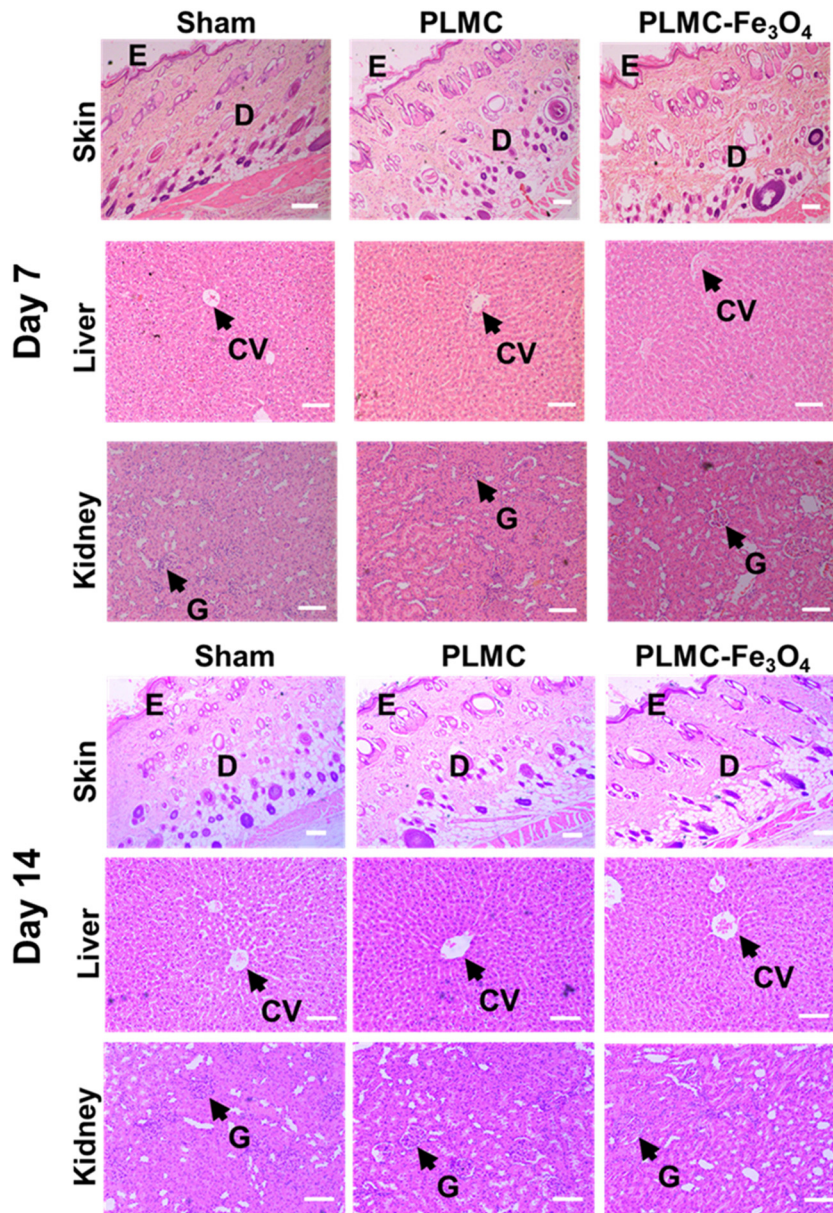
Fig. 7 *In vivo* biological characterization of PLMC and the composite. Histological staining of skin, liver, and kidney sections in the sham, PLMC, and nanocomposite groups on day 7 and day 14 (scale bar is 100 μm for all images except for skin tissues, where the scale bar is 200 μm). E, D in the skin represent epidermis and dermis, CV in liver represents central vein, and G in the kidney refers to glomerulus.

and PLMC–Fe$_3$O$_4$ composites were printed selectively in different regions of the same structure to have sequential and selective stimulation under heating and magnetic field actuation, respectively, to explore applications in soft robotics. These results further demonstrate the versatility of the material system in being able to be printed into a variety of complex shapes, with tailored properties (by varying the nanofiller content), tunable recovery times (by varying the nanofiller content and/or magnetic field strength), and favorable biocompatibility, making it a promising candidate for a variety of patient-specific deployable medical devices. However, long-term degradation studies along with detailed studies of any side effects of the alternating magnetic field as the stimulation are warranted for potential clinical translation of these materials.

Conclusions

In this study, novel PLMC–5% Fe$_3$O$_4$ composites were 3D printed *via* extrusion-based printing. The printed composites exhibited excellent shape fixity ratios ($\approx 95\%$) and shape recovery ratios ($\approx 99\%$) for both 2D and 3D shapes. The key advantages include short recovery times (under 15 s) at physiologically relevant recovery temperatures (≈ 40 °C). The

composites were also printed into porous scaffold-like constructs. These printed structures were compressed into shapes that can be deployed in a minimally invasive manner, magnetically guided, and were recovered ($\approx$99%) by inductive heating to the original shapes. Neat PLMC and PLMC composites were used to print distinct regions in a single structure, which then exhibited selective and sequential recovery through direct and inductive heating. The composites were found to be cytocompatible *in vitro* and biocompatible *in vivo*. The composites exhibited good osteogenic potential, as confirmed through improved mineralization for possible use in the repair and regeneration of bony tissues. These features collectively make the composite materials attractive candidates as deployable biomaterials and for other biomedical applications that require *in situ* triggering of shapes to conformally fill irregular defect dimensions *in vivo*. Taken together, PLMC-based magnetic nanocomposites pave the way for a multitude of applications spanning robotics, advanced manufacturing, biomedical areas, *etc.*, that demand excellent and fast shape recoveries with complex geometries.

Conflicts of interest

The authors have no conflcts of interest to declare.

Acknowledgements

References

1 B. Panda, S. C. Paul, L. J. Hui, Y. W. D. Tay and M. J. Tan, *J. Cleaner Prod.*, 2017, **167**, 281–288.

2 P. M. Bhatt, R. K. Malhan, A. V. Shembekar, Y. J. Yoon and S. K. Gupta, *Addit. Manuf.*, 2020, **31**, 100933.

3 M. Ramola, V. Yadav and R. Jain, *J. Manuf. Technol. Manage.*, 2018, **30**(1), 48–69.

4 J. Choi, O.-C. Kwon, W. Jo, H. J. Lee and M.-W. Moon, *3D Print. Addit. Manuf.*, 2015, **2**, 159–167.

5 G. Scalet, *Actuators*, 2020, **9**(1), 10.

6 Q. Ze, X. Kuang, S. Wu, J. Wong, S. M. Montgomery, R. Zhang, J. M. Kovitz, F. Yang, H. J. Qi and R. Zhao, *Adv. Mater.*, 2020, **32**, 1906657.

7 L. Santo, F. Quadrini, A. Accettura and W. Villadei, *Procedia Eng.*, 2014, **88**, 42–47.

8 J. Delaey, P. Dubruel and S. Van Vlierberghe, *Adv. Funct. Mater.*, 2020, **30**, 1909047.

9 A. Joshi, S. Choudhury, V. S. Baghel, S. Ghosh, S. Gupta, D. Lahiri, G. K. Ananthasuresh and K. Chatterjee, *Adv. Healthcare Mater.*, 2023, **12**, 2300701.

10 L. Sun, W. Huang, C. Wang, Y. Zhao, Z. Ding and H. Purnawali, *J. Polym. Sci., Part A: Polym. Chem.*, 2011, **49**, 3574–3581.

11 X. Yang, L. Wang, W. Wang, H. Chen, G. Yang and S. Zhou, *ACS Appl. Mater. Interfaces*, 2014, **6**, 6545–6554.

12 Y. Wu, J. Hu, C. Zhang, J. Han, Y. Wang and B. Kumar, *J. Mater. Chem. A*, 2015, **3**, 97–100.

13 C. M. Yakacki, R. Shandas, C. Lanning, B. Rech, A. Eckstein and K. Gall, *Biomaterials*, 2007, **28**, 2255–2263.

14 W. M. Huang, C. L. Song, Y. Q. Fu, C. C. Wang, Y. Zhao, H. Purnawali, H. B. Lu, C. Tang, Z. Ding and J. L. Zhang, *Adv. Drug Delivery Rev.*, 2013, **65**, 515–535.

15 W. Small Iv, T. S. Wilson, W. J. Benett, J. M. Loge and D. J. Maitland, *Opt. Express*, 2005, **13**, 8204–8213.

16 J.-J. Hu, Q. Lei and X.-Z. Zhang, *Prog. Mater. Sci.*, 2020, **114**, 100685.

17 X. Wan, H. Wei, F. Zhang, Y. Liu and J. Leng, *J. Appl. Polym. Sci.*, 2019, **136**, 48177.

18 S. Dai, S. Yue, Z. Ning, N. Jiang and Z. Gan, *ACS Appl. Mater. Interfaces*, 2022, **14**, 14668–14676.

19 G. Li, Q. Yan, H. Xia and Y. Zhao, *ACS Appl. Mater. Interfaces*, 2015, **7**, 12067–12073.

20 W. Liu, A. Wang, R. Yang, H. Wu, S. Shao, J. Chen, Y. Ma, Z. Li, Y. Wang and X. He, *Adv. Mater.*, 2022, 2201914.

21 K. Yu, Y. Liu and J. Leng, *RSC Adv.*, 2014, **4**, 2961–2968.

22 G. D. Soto, C. Meiorin, D. G. Actis, P. Mendoza Zélis, O. Moscoso Londoño, D. Muraca, M. A. Mosiewicki and N. E. Marcovich, *Eur. Polym. J.*, 2018, **109**, 8–15.

23 S.-Y. Gu, K. Chang and S.-P. Jin, *J. Appl. Polym. Sci.*, 2018, **135**, 45686.

24 R. Mohr, K. Kratz, T. Weigel, M. Lucka-Gabor, M. Moneke and A. Lendlein, *Proc. Natl. Acad. Sci. U. S. A.*, 2006, **103**, 3540–3545.

25 H. Wei, Q. Zhang, Y. Yao, L. Liu, Y. Liu and J. Leng, *ACS Appl. Mater. Interfaces*, 2017, **9**, 876–883.

26 F. Zhang, L. Wang, Z. Zheng, Y. Liu and J. Leng, *Composites, Part A*, 2019, **125**, 105571.

27 W. Zhao, Z. Huang, L. Liu, W. Wang, J. Leng and Y. Liu, *Compos. Sci. Technol.*, 2021, **203**, 108563.

28 M. Xie, L. Wang, J. Ge, B. Guo and P. X. Ma, *ACS Appl. Mater. Interfaces*, 2015, **7**, 6772–6781.

29 D. Zhang, O. J. George, K. M. Petersen, A. C. Jimenez-Vergara, M. S. Hahn and M. A. Grunlan, *Acta Biomater.*, 2014, **10**, 4597–4605.

30 R. M. Baker, L.-F. Tseng, M. T. Iannolo, M. E. Oest and J. H. Henderson, *Biomaterials*, 2016, **76**, 388–398.

31 X. Wan, Y. He, Y. Liu and J. Leng, *Addit. Manuf.*, 2022, **53**, 102689.

32 M. Bao, X. Lou, Q. Zhou, W. Dong, H. Yuan and Y. Zhang, *ACS Appl. Mater. Interfaces*, 2014, **6**, 2611–2621.

33 X. Zheng, S. Zhou, Y. Xiao, X. Yu, X. Li and P. Wu, *Colloids Surf., B*, 2009, **71**, 67–72.

34 M. C. Righetti, *Materials*, 2017, **10**, 442.

35 A. N. Frone, S. Berlioz, J.-F. Chailan and D. M. Panaitescu, *Carbohydr. Polym.*, 2013, **91**, 377–384.

36 T. Fuoco, T. r Mathisen and A. Finne-Wistrand, *Biomacromolecules*, 2019, **20**, 1346–1361.

37 W. V. Srubar, S. Pilla, Z. C. Wright, C. A. Ryan, J. P. Greene, C. W. Frank and S. L. Billington, *Compos. Sci. Technol.*, 2012, **72**, 708–715.

38 R. G. Ferrillo and P. J. Achorn, *J. Appl. Polym. Sci.*, 1997, **64**, 191–195.

39 S. Sharifi, T. G. van Kooten, H.-J. C. Kranenburg, B. P. Meij, M. Behl, A. Lendlein and D. W. Grijpma, *Biomaterials*, 2013, **34**, 8105–8113.

40 C. Yue, M. Li, Y. Liu, Y. Fang, Y. Song, M. Xu and J. Li, *Addit. Manuf.*, 2021, **46**, 102146.

41 T. Sauter, M. Heuchel, K. Kratz and A. Lendlein, *Polym. Rev.*, 2013, **53**, 6–40.

42 J. L. Hu, F. L. Ji and Y. W. Wong, *Polym. Int.*, 2005, **54**, 600–605.

43 S. Kyle, Z. M. Jessop, A. Al-Sabah and I. S. Whitaker, *Adv. Healthcare Mater.*, 2017, **6**, 1700264.

44 T. Weigel, R. Mohr and A. Lendlein, *Smart Mater. Struct.*, 2009, **18**, 025011.

45 B. A. Evans, M. D. Bausch, K. D. Sienerth and M. J. Davern, *J. Magn. Magn. Mater.*, 2018, **465**, 559–565.

46 M. Ma, Y. Wu, J. Zhou, Y. Sun, Y. Zhang and N. Gu, *J. Magn. Magn. Mater.*, 2004, **268**, 33–39.

47 S. Salkhi Khasraghi, A. Shojaei, M. Janmaleki and U. Sundararaj, *Eur. Polym. J.*, 2021, **159**, 110735.

48 S. Ghasempour, M. A. Shokrgozar, R. Ghasempour and M. Alipour, *Exp. Toxicol. Pathol.*, 2015, **67**, 509–515.

49 T. M. Filion, J. Xu, M. L. Prasad and J. Song, *Biomaterials*, 2011, **32**, 985–991.

50 M.-W. Han and S.-H. Ahn, *Adv. Mater.*, 2017, **29**, 1606580.

51 B. Jin, H. Song, R. Jiang, J. Song, Q. Zhao and T. Xie, *Sci. Adv.*, 2018, **4**, eaao3865.

52 E. Diller and M. Sitti, *Adv. Funct. Mater.*, 2014, **24**, 4397–4404.

53 A. M. Abdullah, X. Li, P. V. Braun, J. A. Rogers and K. J. Hsia, *Adv. Mater.*, 2018, **30**, 1801669.

54 A. Kashirina, Y. Yao, Y. Liu and J. Leng, *Biomater. Sci.*, 2019, **7**, 3961–3983.

55 G. W. Richter, *J. Exp. Med.*, 1959, **109**, 197–216.

56 A. Ali, H. Zafar, M. Zia, I. ul Haq, A. R. Phull, J. S. Ali and A. Hussain, *Nanotechnol., Sci. Appl.*, 2016, **9**, 49–67.

57 A. P. Pêgo, M. J. A. Van Luyn, L. A. Brouwer, P. B. van Wachem, A. A. Poot, D. W. Grijpma and J. Feijen, *J. Biomed. Mater. Res., Part A*, 2003, **67A**, 1044–1054.

58 M. N. Hassan, M. A. Yassin, A. M. Eltawila, A. E. Aladawi, S. Mohamed-Ahmed, S. Suliman, S. Kandil and K. Mustafa, *Biomater. Res.*, 2022, **26**, 55.

59 S. J. H. Soenen, N. Nuytten, S. F. De Meyer, S. C. De Smedt and M. De Cuyper, *Small*, 2010, **6**, 832–842.